Numerical Analysis of Dynamic Instability at Transonic Speeds

By

Susumu TERAMOTO,* Kozo FUJII[†], and Kouju HIRAKI[†]

(1 February 2003)

Abstract: A flat capsule with blunt nose like Muses-C reentry capsule tends to be dynamically unstable at transonic speeds. This instability phenomena has been studied experimentally since 1960's, but its mechanism is not well understood. The flowfield around the reentry capsule is numerically simulated and discussed to reveal the mechanism of the dynamic instability. A new post-processing technique that uses frequency filters, are applied to detect the flow structure out of complicated flowfield.

The results showed that the base pressure of the capsule produces pitch-down moment for the positive pitch angle, and the oscillation of the base pressure is delayed from the pitch angle when the capsule oscillates in pitch. The delay cause the hysteresis in the aerodynamic pitching moment, and the hysteresis makes the capsule dynamically unstable. The base pressure and the wake at the neck point (the foot of the recompression shock wave) oscillate with the same delay time. When the neck point moves upward, the pressure at the upper part of the base becomes higher and the base pressure produces pitch-down moment. Two oscillations coincides each other, and therefore the base pressure is correlated to the flowfield near the neck point.

There is strong reverse flow behind the capsule, and the impingement of the reverse flow against the base determine the base pressure distribution. The behavior of the reverse flow is governed by the vortex structure behind the capsule. The vortex is composed of the ring vortex and the pair of longitudinal vortices, and the interaction between the longitudinal vortices and the flowfield near the neck point define the base pressure distribution. The base pressure does not change until the disturbance of the longitudinal vortices caused by the pitching motion of the capsule reaches the neck point, and the time lag is the cause of the phase delay of the base pressure.

Both the base pressure distribution and the delay of the base pressure is governed by the pair of longitudinal vortices, and therefore the dynamic stability of the capsule is closely related to the formation of the pair of longitudinal vortices.

1.   INTRODUCTION

One of the most distinctive features of the Muses-C mission is the reentry velocity of the sample return capsule. Since the return capsule reenter directly into the earth's atmosphere,

* University of Tokyo Department of Aeronautics and Astronautics, 7-3-1 Hongo, Bunkyo-ku, Tokyo 113-8656, Japan
† The Institute of Space and Astronautical Science, 3-1-1 Yoshino-dai, Sagamihara, Kanagawa 229-8510, Japan
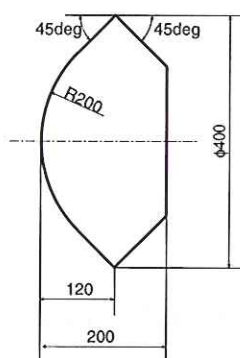
Fig. 1: Outline configuration of the reentry capsule of the Muses-C.

the reentry velocity is as high as 12 km/s, and the maximum heating rate is expected to reach 16-18 MJ/m^2, therefore heat protection is the most important issue in the design of the sample return capsule. Figure 1 shows preliminary configuration of the reentry capsule of the Muses-C. Large nose radius produce large drag, and short body length reduce the weight, resulting the small ballistic coefficient. In general, lowering the mass-to-drag ratio reduces the maximum convective heating rate therefore short and blunt capsule is preferable for the heat protection. However, such capsules tend to be dynamically unstable and sometimes enter self-excited oscillation at transonic speeds. These factors also needs to considered in the design of sample-return missions.

This type of dynamic instability has been known and studied since the 1960's (Wright and Kilgore, 1966, Sammonds and Kruse, 1975, Yoshinaga et al., 1996, Berner and Winchenbach, 1998, Chapman and Yates, 1998), yet the detailed mechanism remains largely unknown. The interesting feature of this instability phenomenon is that the reduced frequency defined by the body diameter and the uniform flow velocity is as low as $O(0.01)$. This experimental result, along with the fact that the instability only occurs at transonic speeds, indicates that high-frequency perturbations such as unsteadiness caused by vortex shedding from the edge of the capsule, are not the primary sources of the instability. Recently, Hiraki (Hiraki et al., 1998) studied the phenomena experimentally using a one-dimensional free oscillation method, and revealed that the dynamic instability is caused by a delay of the base pressure of the capsule.

Despite these studies, the detailed mechanism of the dynamic instability at transonic speeds is not well understood. The purpose of the present study is to reveal the mechanism of the dynamic instability.

2.   METHOD OF ANALYSIS

For the analysis of the mechanism of the dynamic instability, we choose computational fluid dynamics (CFD) approach as it gives us the time-dependent information of the flowfield away from the capsule, where seems to dominate the dynamic instability phenomena.

The capsules examined in the current study are the same as those used in Hiraki's experiment. The forebody is composed of a blunt cone with a spherical nose, and the afterbody is a truncated cone with a flat base. The geometric parameters of the capsules are listed in Table 1, and the D45 model capsule is shown in Fig. 2. The wind-tunnel experiment revealed that the D45 model is dynamically unstable at a small angle of attack and it enters self-excited
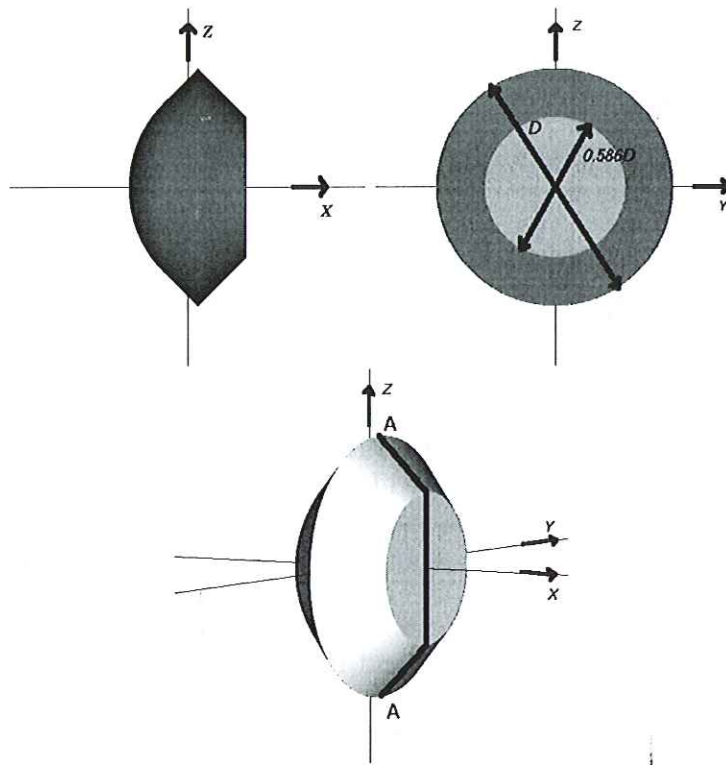
Fig. 2: **D45 model capsule.**

Table 1: Geometry of model capsules.

	D45 model	D30 model
Nose radius	50 mm	
Semi-apex angle	45°	30°
Maximum diameter	100 mm	
Body length	50 mm	
Base configuration	45° truncated cone	
Dynamic stability at transonic speeds	unstable	stable

oscillation at transonic speeds, while the D30 model is dynamically stable at all speeds between $M = 0.3 \sim 2.5$.

As it is difficult to discuss the complicated unsteady flowfield directly, the mechanism of the dynamic instability is discussed based on a step-by-step approach. The characteristics of the flowfield around the capsule under forced oscillation is discussed. Then the flowfields around the oscillating capsule are compared with those around the capsule at fixed pitch angles, and new flow model is proposed based on the observations. Using this model, the flowfield for the oscillating capsule is discussed based on that for the capsule at fixed pitch angle, and the correlation between the flowfield and the base pressure is discussed in detail. Finally, the

mechanism of the dynamic instability is discussed based on the proposed model.

2.1 Numerical method

The governing equations employed here are the Reynolds-averaged unsteady three-dimensional thin-layer Navier-Stokes equations:

$$\partial_t \hat{Q} + \partial_\xi \hat{E} + \partial_\eta \hat{F} + \partial_\zeta \hat{G} = \partial_\zeta \hat{S}_V$$

Length, density and velocity are normalized by the diameter of the capsule and the density and speed of sound of the uniform flow, respectively.

Numerical fluxes for the convective terms are evaluated by the SHUS scheme (Simple High-resolution Upwind Scheme) (Shima and Jounouchi, 1997) and it is extended to higher-order by the MUSCL interpolation based on the primitive variables. The LU-ADI factorized implicit algorithm (Obayashi et al., 1986) is employed for time integration. Experience has shown that the LU-ADI scheme has sufficient temporal accuracy to resolve the behavior of large-scale vortex structures provided that the local CFL number is smaller than unity outside the boundary layer. The grid spacing and the time step are carefully chosen in the present study so as to maintain sufficient temporal accuracy to resolve the temporal behavior of the flowfield. The flowfield is considered to be fully turbulent and Baldwin-Lomax's algebraic turbulence model (Baldwin and Lomax, 1978) is applied near the solid wall.

The computational grid used in the simulation is and $121 \times 64 \times 61$ for the analysis of the oscillating capsule. and $151 \times 64 \times 121$ for the fixed capsule. The minimum grid spacing near the wall is 2.0×10^{-5}, and the wall coordinate y^+ at the first grid point is less than 2 for the most part of the capsule surface such that at least one grid point is distributed inside the laminar sublayer. The computational domain is -4.0 to 10.0 in the x direction and -10.0 to 10.0 in the y and z directions. The entire grid system oscillates around the center of gravity of the capsule for the simulation of the flowfield around the oscillating capsule. A grid sensitivity study (Teramoto et al., 2001) showed that a coarser $121 \times 64 \times 81$ grid is sufficiently fine to resolve the unsteady behavior of the flowfield behind the capsule. However, a finer grid is used for the simulation of the cases with fixed pitch angle to improve the spatial resolution and reveal the detailed flow mechanism.

Table 2 shows the flow conditions, corresponding to those of Hiraki's wind-tunnel experiment (Hiraki et al., 1998). The time step Δt for the simulation of the flowfield around the oscillating capsule is 1/150,000 of one oscillation cycle, and that for the capsule at fixed pitch angle is set at 0.001 in units of non-dimensional time. For both cases, Δt is approximately 3.4×10^{-7} second in physical time. The numerical results indicate that the highest dominant frequency of the flowfield is approximately 1 kHz, corresponding to the Strouhal number ($St = fD/u$) of 0.27. Therefore, $\Delta t = 3.4 \times 10^{-7}$ second is sufficiently small to resolve the unsteady fluctuation of the flowfield.

The simulations were carried out on the Fujitsu VPP800/12 at the ISAS. The computation required 20 hours on 4 processing elements (PEs) of VPP800/12 for one forced oscillation cycle. The simulations for the fixed pitch angle were carried out on a single PE, and each case required approximately 30 hours.

2.2 Postprocessing

Figure 3 shows the time history of the base pressure of the D45 model fixed at $\alpha = 10°$. High-frequency fluctuation of approximately 1 kHz is observed with amplitude reaching 10% of the

Table 2: Flow conditions.

Mach number	1.3
Dia. of capsule	0.1 m
Re number	2.5×10^6
Frequency	20 Hz
Max. pitch angle	$\pm 20°$
Reduced frequency	0.03
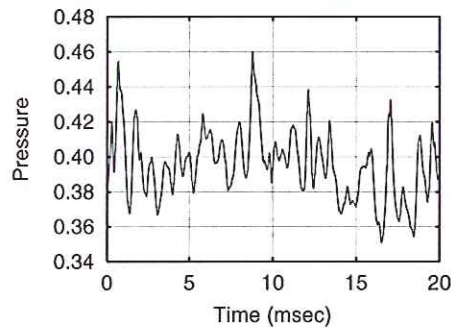
Fig. 3: Time history of base pressure of D45 model fixed at $\alpha = 10°$.

average pressure. This high-frequency fluctuation is also observed in the simulation of forced pitching oscillation, and is considered to represent the shedding of small vortices from the edge of the capsule.

As the time scale of the vortex shedding (1 kHz) is very different from that of the oscillation of the capsule (20 Hz), the low frequency oscillation of the capsule does not appear to be related to the high-frequency shedding of small vortices. The behavior of the small vortices is therefore expected to be the same for both the capsule fixed at a certain pitch angle and the oscillating capsule. The difference between the flowfield around the fixed capsule and the oscillating capsule is the primary concern in the current study, and therefore the influence of the high-frequency component will be excluded in the analysis.

For simulation of the cases with fixed pitch angle, the physical properties are averaged over 20,000 steps (approximately 7 msec in the real time units, sufficient to exclude the disturbance at 1 kHz) after the flowfield has reached the stationary state, and the time-averaged properties are used for discussion. The physical properties obtained from the unsteady simulation of the forced oscillation are processed by a low-pass filter (LPF) with a cut-off frequency of 150 Hz in order to eliminate the high-frequency fluctuation. The dominant frequency of the flowfield is 20 Hz, which is sufficiently low compared to the cut-off frequency to avoid distortion of the fundamental behavior of the flowfield by the LPF. The details and usefulness of this filtering method are described in Reference (Teramoto and Fujii, 2001).
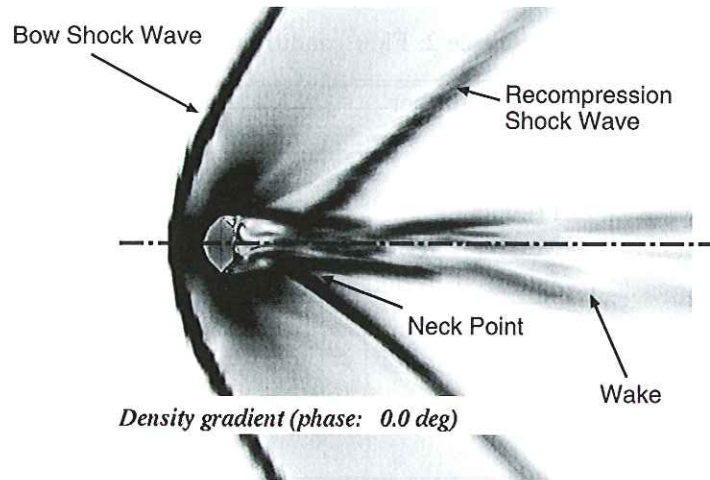
Fig. 4: Instantaneous density gradient distribution.

3. FLOWFIELD AROUND THE CAPSULE IN THE PITCHING OSCILLATION

3.1 Overview of the Flowfield

Figure 4 shows the instantaneous density gradient distribution around the capsule in the forced pitching oscillation. The capsule is at zero angle of attack, and it is in the pitch-up motion at the moment of the Fig. 4 The bow shock wave is formed ahead of the capsule. The flow separates at the edge of the capsule and forms shear layer behind the capsule. The shear layer converges as it goes downstream due to the strong expansion at the edge, and the recompression shock wave emanates from the neck point of the wake. The oscillation of the flowfield is shown in Fig. 5. The fundamental flow features do not change even when the capsule oscillates, although their locations move with the pitch angle of the capsule; the upper half of the bow shock wave moves backward and lower part moves forward, and the wake downstream moves upward, when the capsule is pitched up. Figure 5 also shows that the flowfield oscillates with hysteresis. The wake passes slightly below the centerline when the capsule is pitching up at $\alpha = 0°$, while it passes upper side when the capsule is pitching down at $\alpha = 0°$. The flowfield downstream varies depending on the direction of the pitching motion of the capsule.

The flowfield behind the capsule is essentially unsteady due to the vortex shedding from the edge of the capsule. The power spectrum density of the base pressure of the capsule in the forced pitching oscillation (20Hz) and that of the capsule fixed at zero angle of attack are compared in Fig.6. The base pressure of the capsule fixed at $\alpha = 0°$ oscillates at approximately 770Hz, which corresponds to the Strouhal number $St = 0.256$, due to the vortex shedding and no distinct peak is observed below 400Hz. Figure 6 shows that the lowest natural frequency of the flowfield is 770Hz for this flow configuration. When the capsule oscillates in pitch at 20Hz, the peak that corresponds to the vortex shedding shifts higher to 1000Hz, and new peaks appear at 20Hz and 40Hz. These peaks are the harmonic fluctuation induced by the pitching motion of the capsule. Although high frequency fluctuation is noticeable behind the capsule, its frequency is far higher than that of the oscillation of the capsule, and it seems that the high frequency disturbance does not directly contribute to the dynamic instability of the capsule.
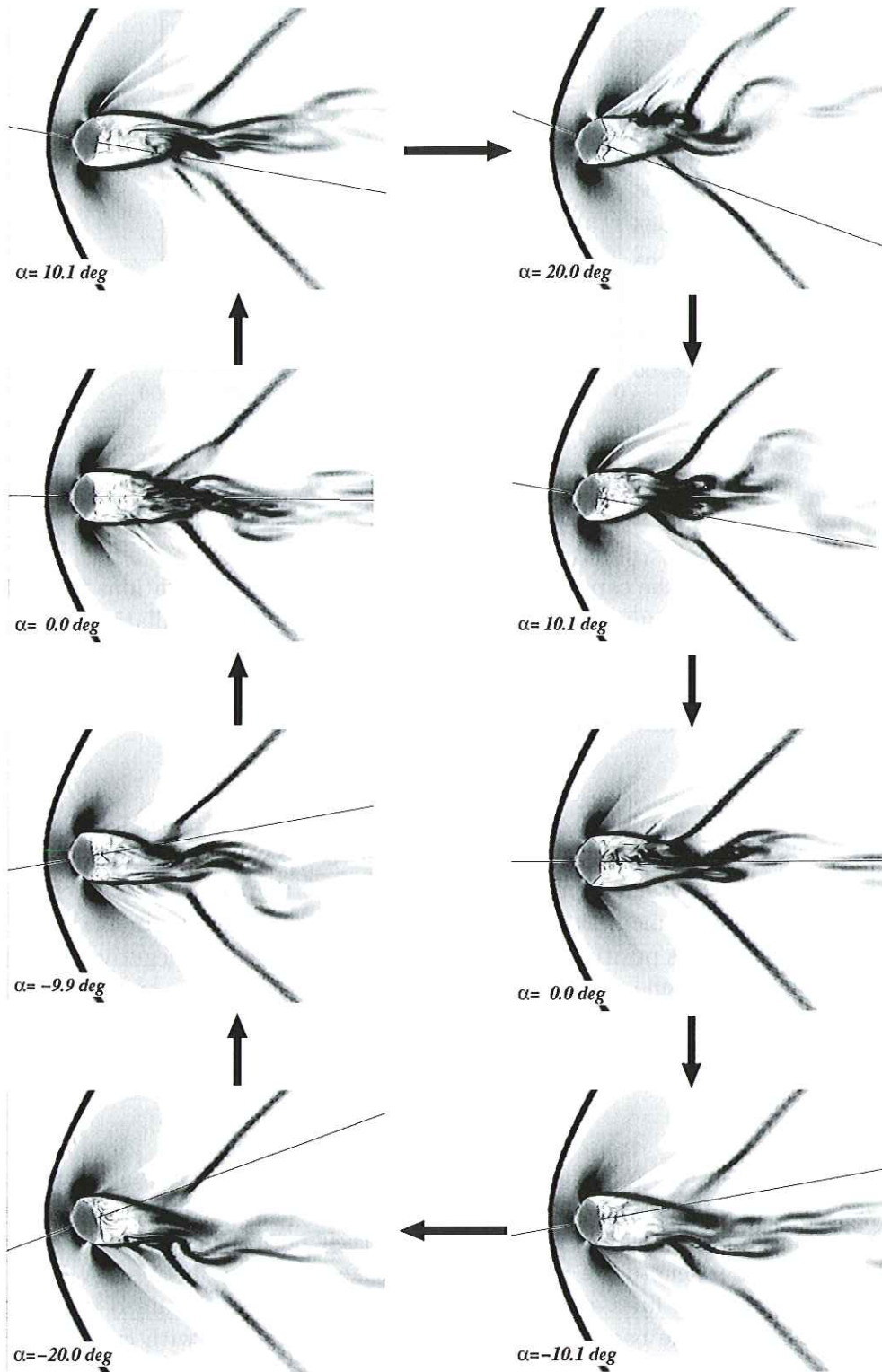
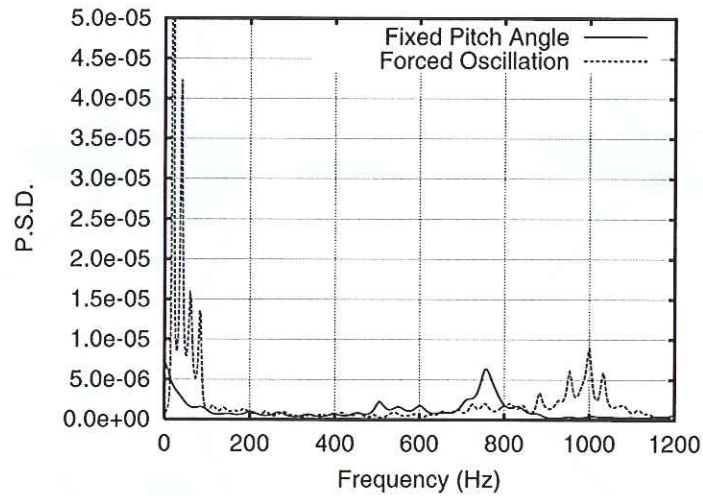Fig. 5: Flowfield around the oscillating capsule.

Fig. 6: Power spectrum density of the base pressure.

The pitching oscillation of the capsule induces only the harmonic fluctuations to the flowfield, and therefore we can focus only on the harmonic component of the oscillation of the flowfield in the following discussions.

3.2   Pitching Moment and Surface Pressure

Pitching Moment

The aerodynamic pitching moment around the axis of rotation is plotted against the pitch angle in Fig. 7. The gradient of the moment, $\frac{\partial M}{\partial \theta}$ is negative. The aerodynamic moment works to suppress the pitch angle of the capsule, therefore the capsule is statically stable in the pitch. Hysteresis of the moment is also observed in Fig. 7. The pitching moment is higher when the angular velocity is positive than when the angular velocity is negative. Consequently, net work-input to the capsule during one oscillation cycle is positive, and the amplitude of the oscillation grows up. The capsule is dynamically unstable under this enforced oscillation although it is statically stable.

Surface Pressure

Time histories of the surface pressure at two locations; one in the front and the other in the base part of the capsule, are plotted with the history of the pitch angle in Fig. 9. Both are located in the plane of symmetry of the capsule, and their positions are shown in Fig. 8. The cross symbols in Fig. 9 denote the instantaneous surface pressure obtained by the numerical simulation, and the dashed lines are the first harmonic component obtained from the Fourier analysis. The history of the base pressure is processed by the LPF with cut-off frequency of 150Hz to eliminate high frequency fluctuations.

The surface pressure at the front point varies synchronously with the pitch angle; the pressure is same at the same pitching angle both in the pitching up and down. Therefore, the front pressure does not contribute to the hysteresis of the pitching moment. On the other hand, the base pressure oscillates with a phase delay against the pitch angle. The base pressure at
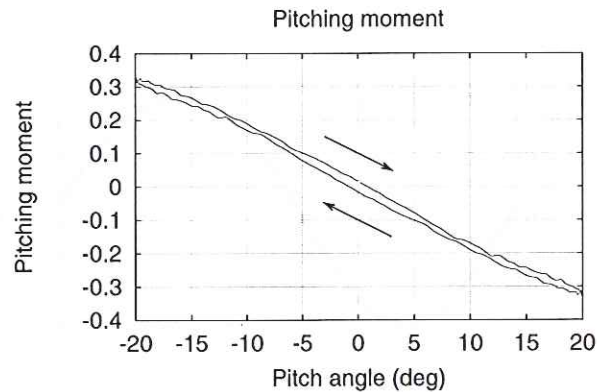
Pitching moment

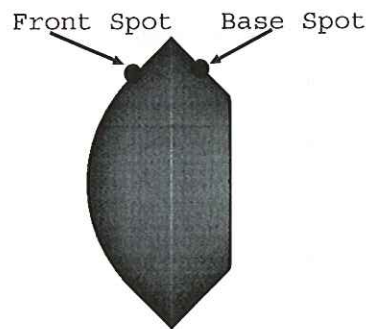Fig. 7: Pitching moment works to the capsule.

Fig. 8: Location of pressure port.

a certain pitch angle varies depending on the direction of the pitching motion and hence, the pitching moment due to the base pressure shows hysteresis. The pressure at the upper part of the base is higher when the pitch angle is positive, and the higher static pressure at the base rotates the capsule pitching-down. The base pressure works on the capsule to make it statically stable. In general, a system that is statically stable becomes dynamically unstable when the system works with delay, and therefore the phase delay of the base pressure makes the capsule dynamically unstable.

The dynamic instability of the capsule is caused by the hysteresis of the pitching moment, and it is the phase delay of the backside pressure that produces the hysteresis.

3.3 Fluctuation of the Pressure Field

The physical properties are defined on the moving grid fixed to the capsule, however the grid system fixed to the space is sometimes more convenient for the discussion of the flowfield away from the capsule. The physical properties are mapped over the equally spaced rectangular grid fixed to the space, and time histories of the static pressure at all the nodes are processed by the Fourier analysis, and the spatial distribution of the amplitude and the phase are obtained. Figure 10 shows the distribution of the phase angle of the oscillation of the static pressure.
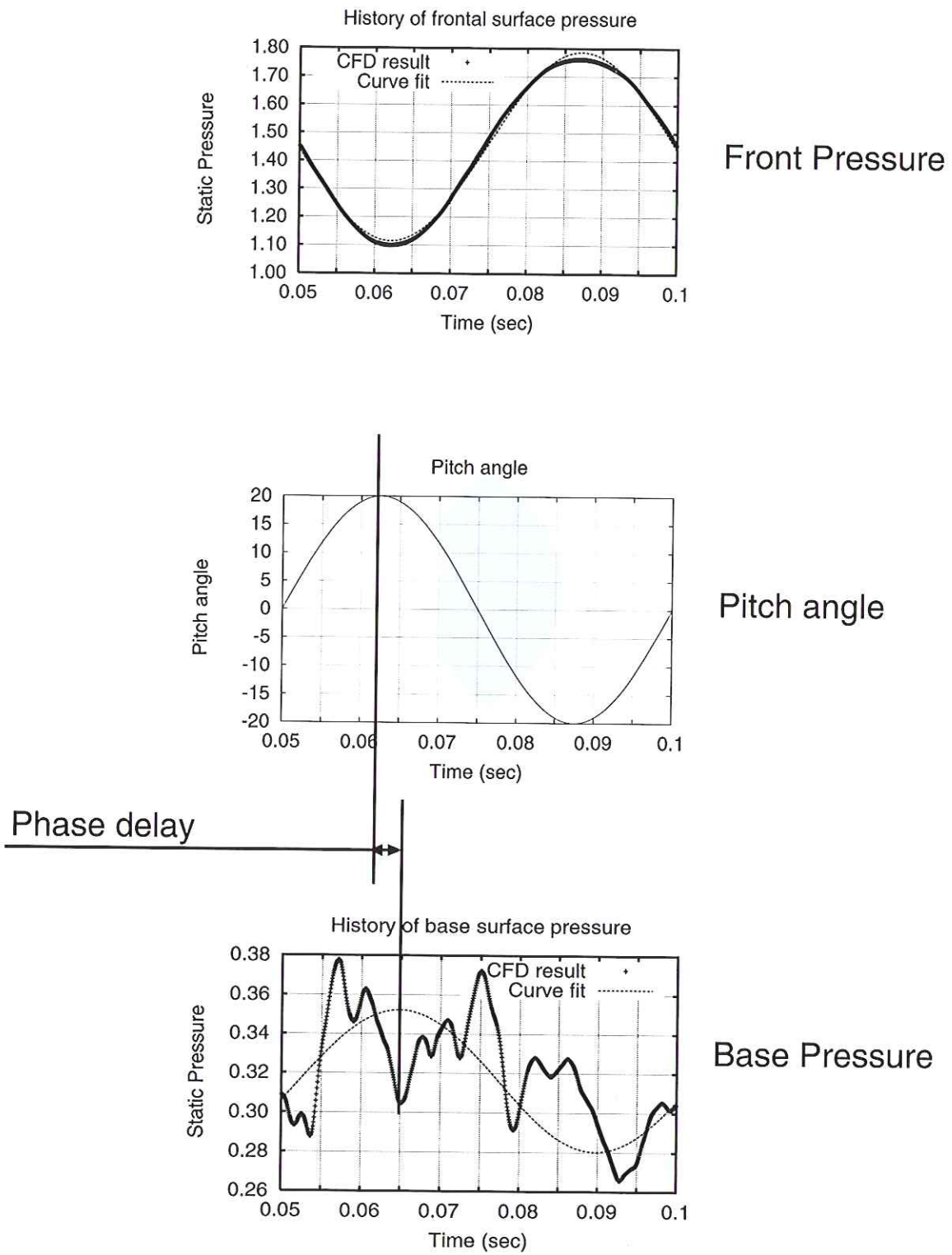
Teramoto et al.

History of frontal surface pressure

Front Pressure

Pitch angle

Pitch angle

Phase delay

History of base surface pressure

Base Pressure

Fig. 9: History of surface pressure.

Only the region where the phase angle is between $-20°$ and $+20°$ is displayed, and the white region indicates the area where the phase is delayed. The contour plots of the density gradient are plotted in the bottom half for reference. The pressure phase along the dashed lines A and B in Fig. 10 are plotted in Figs. 11 and 12 respectively.

The flowfield can be divided into following three regions:

Region 1: The recirculating region surrounded by the capsule, shear layer and the recompression shock wave

Region 2: Wake region downstream of the recompression shock wave

Region 3: Flowfield outside of the wake

Figures 10 to 12 show that the pressure phase is delayed only in the Region 1. The flowfield is supersonic at the Region 3, and the pressure at this region is directly influenced by the upstream flowfield which is coupled with the attitude of the capsule. Therefore the phase delay angle at the this region is almost zero. Figure 12 shows that the phase angle is nearly constant inside both the Region 1 and Region 3, and it changes rapidly at the shear layer at $Z/D \simeq 0.5$. The gradient of the phase angle at the shear layer is as large as 14 (rad/m). One-dimensional propagation of a disturbance wave is described as

$$f(x,t) = f_0 e^{i\omega\left(t - \frac{x}{C}\right)}$$

where i is the imaginary unit and C is the speed of the wave. The phase angle ϕ is given by

$$\phi(x,t) = \omega\left(t - \frac{x}{C}\right)$$

therefore the spatial gradient of the phase angle caused by the propagation is

$$\frac{\partial \phi}{\partial x} = \frac{\omega}{C} = \frac{2\pi f}{C}$$

The flowfield considered in this study is transonic, and the value of the characteristic speeds u, c and $u \pm c$ are all hundreds m/s. If the pressure fluctuations at the Region 1 and the Region 3 are directly correlated each other, the gradient of the phase angle should be $\frac{2\pi f}{c} \simeq 0.4 (\text{rad/m})$ at the interface of two regions, therefore the gradient of 14(rad/m) along the line B is unreasonably large for the transonic flowfield. It indicates that the fluctuation inside the Region 1 is not directly influenced by the fluctuation at the Region 3. The pressure at the Region 2 oscillates with the phase angle approximately 160°, which is 20° delayed against 180°. The pressure at the Region 2 decreases when the capsule pitches up, but the its oscillation is slightly delayed from the pitch angle, and the delay time is same as that at the Region 1. Since the pressures at two regions oscillate with the same delay time, the pressure right behind the capsule is considered to be coupled with the flowfield downstream of the neck point.

3.4 Oscillation of the Shock Wave and the Wake

The amplitude and the phase of the fluctuation of the radial position of the wake along the section B-B in Fig. 13 are shown in Table 3. The wake at the section B-B represents the interface between the Region 1 and Region 3. Since the position of the capsule's edge moves when the capsule oscillates, the deviation of the edge position is subtracted from that of the
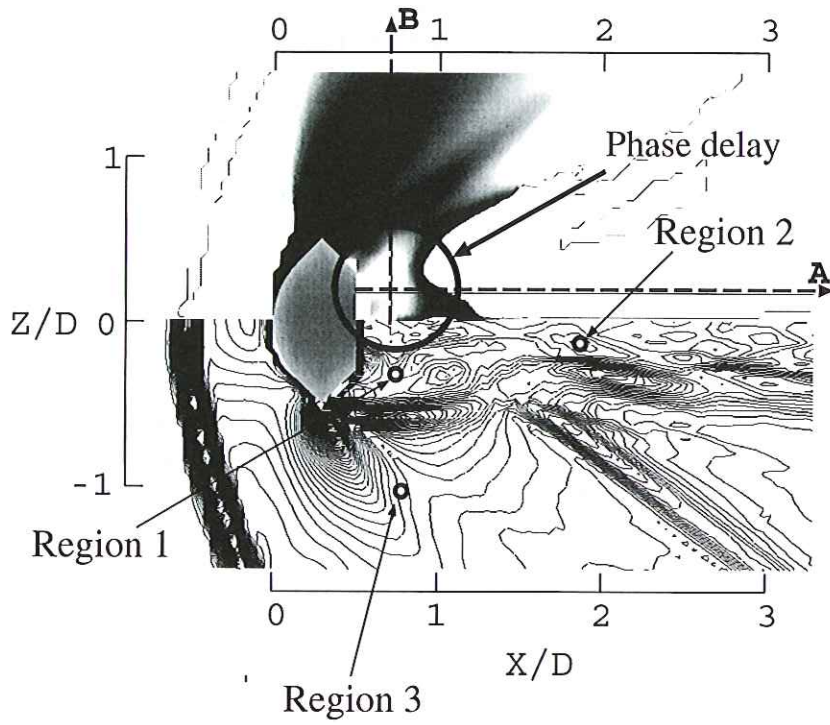
Fig. 10: Top: Pressure phase distribution, Bottom: Density gradient distribution.
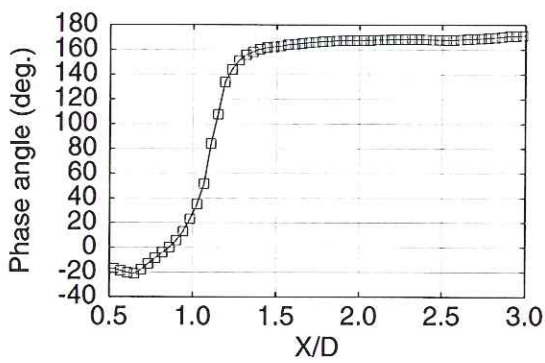

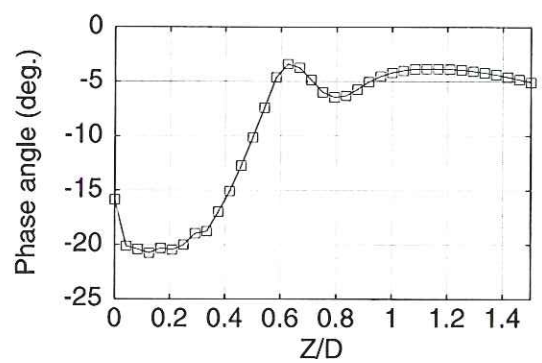Fig. 11: Pressure phase along line A.
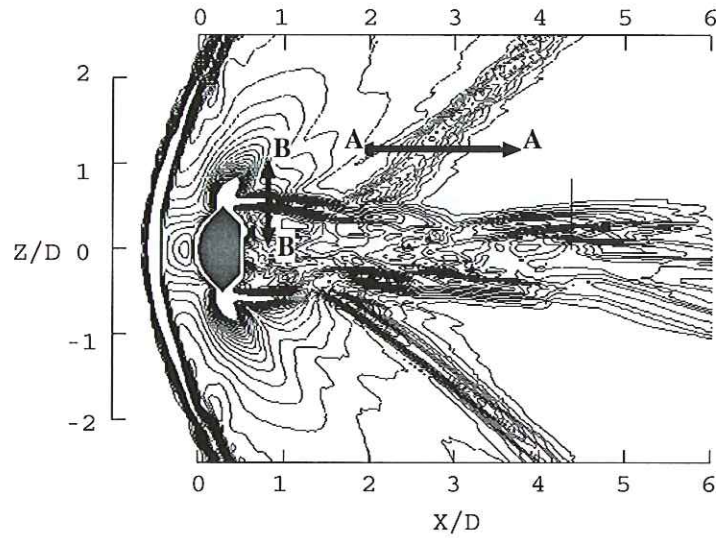

Fig. 12: Pressure phase along line B.

Fig. 13: Definition of the sections.

Table 3: Oscillation of the wake near the capsule.

	Amplitude	Phase
Section B-B	0.016	-98.40 deg

wake position at the analysis of the phase and the amplitude. The amplitude of the oscillation is less than 2% of the diameter of the capsule, and it does not seem that the oscillation of the wake near the capsule directly influences the pressure phase behind the capsule.

Secondly, the axial location of the recompression shock wave along the section A-A in Fig. 13 is plotted against time in Fig. 14. The recompression shock wave oscillates twice during one cycle of the oscillation of the capsule (0.05 sec). The recompression shock wave takes its most backward position 2.2 msec after the capsule passes the neutral (pitch angle $\theta = 0$) position. Thus, the motion of the recompression shock wave is 2.2 msec delayed from the capsule. The delay time of the recompression shock wave coincides with that of the oscillation of the static pressure at Region 1 and Region 2. Since the recompression shock wave emanates from the neck point, the motion of the shock wave represent the oscillation of the flowfield near the neck point.

The pressure inside the Region 1 and Region 2, and the flowfield around the neck point, which is the interface between two regions, all oscillate with the same delay time. Again, the pressure behind the capsule is considered to be coupled with the flowfield around the neck point.
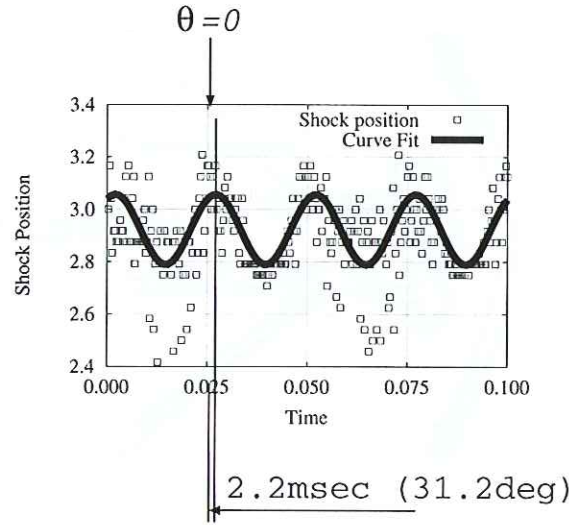
Fig. 14: Shock location along line A-A.

4. EVALUATION OF THE DYNAMIC CHARACTERISTICS BY A SIMPLE CONSTANT-DELAY MODEL

4.1 Aerodynamic forces and base pressure

The characteristics of the base pressure and the aerodynamic pitching moment caused by the base pressure are discussed first.

Time-averaged base pressure distributions for capsule at fixed pitch angle

The time-averaged base pressure distributions along the centerline (line A-A in Fig. 2) are plotted against the z-coordinate for several fixed pitch angles in Fig. 15. The base pressure of the D45 model (Fig. 4.1) decreases uniformly in the region $z < 0.3$ (lower side of the base) as the angle of attack increases. The pressure at $z > 0.3$ also decreases, but to a lesser degree. The pressure difference between $z < 0.3$ and $z > 0.3$ increases as the angle of attack increases. On the other hand, the base pressure of the D30 model is almost uniform, even when the pitch angle is positive (Fig. 4.1).

The difference in the base pressure distributions can be discussed more clearly using the aerodynamic pitching moment. The overall aerodynamic pitching moment due to the surface pressure acting on the capsule is given by $M = \oint p\vec{n} \times \vec{r} \cdot ds$. Here, the contributions from the front pressure and base pressure are discussed separately to account for considerable difference between the flowfields at the front and back of the capsule. The total pitching moment is therefore given by

$$M = M_f + M_b \tag{1}$$

where M_f and M_b are the pitching moments of the front and base, expressed as

$$\begin{cases} M_f(\alpha) & = & \oint_{\text{front area}} p\vec{n} \times \vec{r} \cdot ds \\ M_b(\alpha) & = & \oint_{\text{base area}} p\vec{n} \times \vec{r} \cdot ds \end{cases} \tag{2}$$
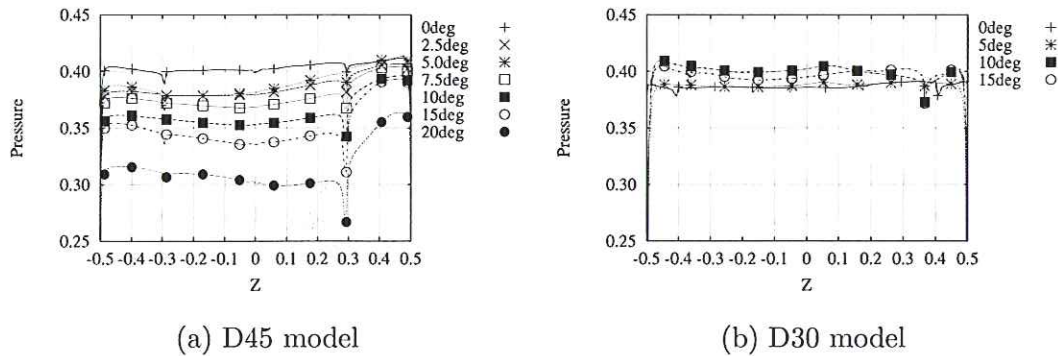
(a) D45 model   (b) D30 model

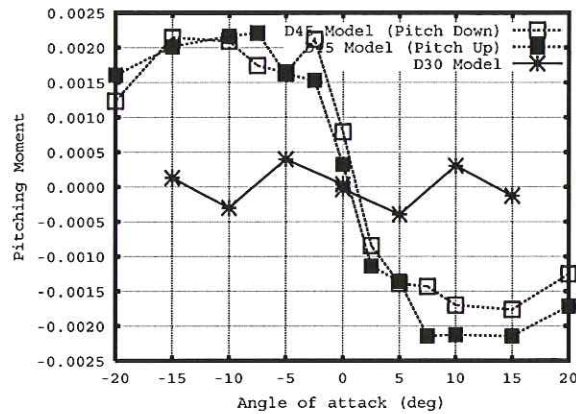Fig. 15: Time-averaged base pressure for fixed pitch angle.

Fig. 16: Base pitching moment of D45 and D30 models (fixed pitch angle).

Figure 16 shows the variation in M_b with pitch angle. Two curves, one for when the capsule quasistatically pitches up and another for when it quasistatically pitches down, are shown for the D45 model. Here, "quasistatic" means that a converged solution at a certain (fixed) pitch angle is used as the initial flowfield for simulation at the next pitch angle.

The base pitching moment of the D45 model is positive (pitch up) for negative pitch angles, and negative for positive pitch angles. The base pressure distributions shown in Fig. 15(a) indicate that the high-pressure region at $z > 0.3$ (upper side of the base)is the origin of the pitch-down moment. Note that the two curves for the D45 model coincide, and there is no sign of static hysteresis.

The base pitching moment of the D30 model is almost flat, which is consistent with the uniform pressure distributions shown in Fig. 15(b).

Evaluation of dynamic characteristics based on static base pressure distributions

Suppose that the surface pressure of the capsule oscillates with a delay time δ with respect to the pitch angle (hereafter, this assumption is named "constant-delay model"). Considering a capsule oscillating in pitch with $\alpha = \alpha_{\mathrm{MAX}} \sin(\omega t)$, the aerodynamic pitching moment acting

on the capsule during the oscillation may be described as

$$M_{f\,\text{delay}}(t) \;=\; M_{f\,\text{fixed}}\left(\alpha_{\text{MAX}}\sin(\omega(t-\delta_f))\right) \tag{3}$$

$$M_{b\,\text{delay}}(t) \;=\; M_{b\,\text{fixed}}\left(\alpha_{\text{MAX}}\sin(\omega(t-\delta_b))\right) \tag{4}$$

where the subscript "fixed" denotes the moment that acts on the capsule at a fixed pitch angle, and "delay" denotes the constant-delay model. Here, $M_{b\,\text{fixed}}$ depends only on the pitch angle because there is no static hysteresis. The result of the forced-oscillation simulation (Teramoto et al., 2001) showed that $\delta_f \simeq 0$ and $\omega\delta_b \ll 1$, then

$$
\begin{aligned}
M_{(t)} \;=\;& M_{f\,\text{delay}}(t) + M_{b\,\text{delay}}(t) \\
\;=\;& \left(M_{f\,\text{fixed}(\alpha)} + M_{b\,\text{fixed}(\alpha)}\right) - \delta_b \left.\frac{\partial M_{b\,\text{fixed}}}{\partial \alpha}\right|_\alpha \dot{\alpha} \\
& + \; O(\alpha^2)
\end{aligned}
\tag{5}
$$

The aerodynamic pitching moment acting on the object in a uniform flow is expressed using the aerodynamic coefficients as follows.

$$M = \frac{1}{2}\rho_\infty u_\infty^2 S D \cdot \left(C_m + (C_{mq} + C_{m\dot{\alpha}})\frac{D}{u_\infty}\dot{\theta}\right) \tag{6}$$

Note that $\theta = \alpha$ since the object is placed in the uniform flow. Comparing Eqs.(5) and (6), following relations are obtained.

$$C_m \;\propto\; M_{f\,\text{fixed}}(\alpha) + M_{b\,\text{fixed}}(\alpha) \tag{7}$$

$$C_{mq} + C_{m\dot{\alpha}} \;\propto\; -\delta_b \left.\frac{\partial M_{b\,\text{fixed}}}{\partial \alpha}\right|_\alpha \tag{8}$$

Since M_f is much larger than M_b, Eqs. (7) and (8) indicate that the static aerodynamic characteristic of the capsule depends mainly on M_f, while the dynamic characteristic is mainly determined by the gradient of M_b. Both Hiraki's experiment (Hiraki et al., 1998) and the authors' numerical study (Teramoto et al., 2001) showed that the dynamic instability of the capsule is caused by the delay of the base pressure. These results support the observation derived from Eq. (8).

The gradient of M_b can be directly evaluated from the simulations of the flowfield around the capsule at fixed pitch angles. The dynamic characteristic of the capsule can then be determined without the simulation of forced oscillation provided that the base pitching moment M_b during the forced oscillation can be approximated by the constant-delay model.

Comparison with simulation results for forced oscillation

The base pitching moment of the D45 model shown in Fig. 16 can be approximated by a function of α as follows.

$$
M_{b\,\text{fixed}}(\alpha) = \begin{cases}
a_M \tanh(b_M\alpha) & |\alpha| < \alpha_{M0} \\
c_M(\alpha - \alpha_{M0}) + a_M\tanh(b_M\alpha_{M0}) & \alpha > \alpha_{M0} \\
c_M(\alpha + \alpha_{M0}) - a_M\tanh(b_M\alpha_{M0}) & \alpha < -\alpha_{M0}
\end{cases}
\tag{9}
$$

$$c_M = a_M b_M (1 - \tanh^2(b_M\alpha_{M0}))$$

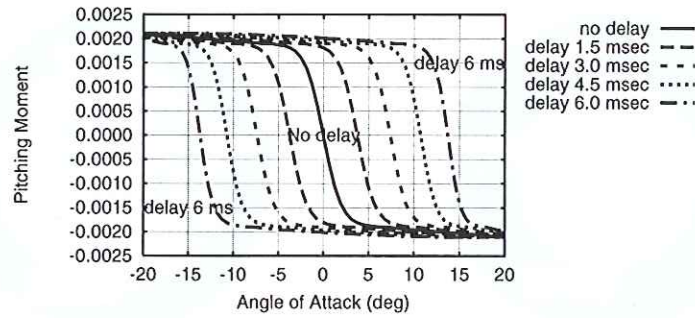$$a_M = -0.0019, \quad b_M = 0.5, \quad \alpha_{M0} = 5.5$$

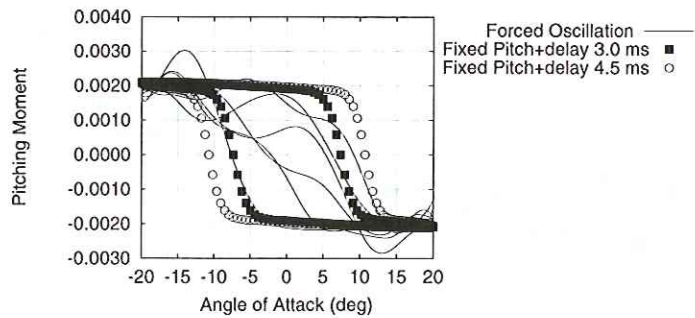Fig. 17: Base pitching moment of D45 model (constant-delay model).

Fig. 18: Base pitching moment of D45 model (forced oscillation)

Substituting Eq. (9) into Eq. (4), the pitch moments $M_{b\text{delay}}$ are plotted for several values of δ_b in Fig. 17. The curves show the time histories of M_{bdelay} evaluated by the constant-delay model for delay times of 1.5, 3.0, 4.5 and 6.0 msec. The solid curve in Fig. 18 shows the actual history of the base pitching moment M_b for the D45 model capsule in forced pitching oscillation. The histories of M_{bdelay} evaluated from the constant-delay model are plotted as symbols in the figure. The magnitude of M_b remains almost constant at ± 0.002 up to a certain angle of attack, at which M_b reverses in sign. The M_b curves are close to the plots of the simple constant-delay model for a delay time of roughly $\delta = 3.0$ msec, although the delay time is scattered between cycles.

The base pitching moment during the forced oscillation is reasonably approximated by the simple constant-delay model. The characteristic of the base pressure distribution reflects the behavior of the flowfield behind the capsule, and therefore the agreement of M_b indicates that the flowfield behind the oscillating capsule can also be expressed by the constant-delay model. That is, the mechanism of the flowfield that determines the base pressure distribution of the oscillating capsule is essentially the same as that for the capsule at a fixed pitch angle with the delay time in mind.
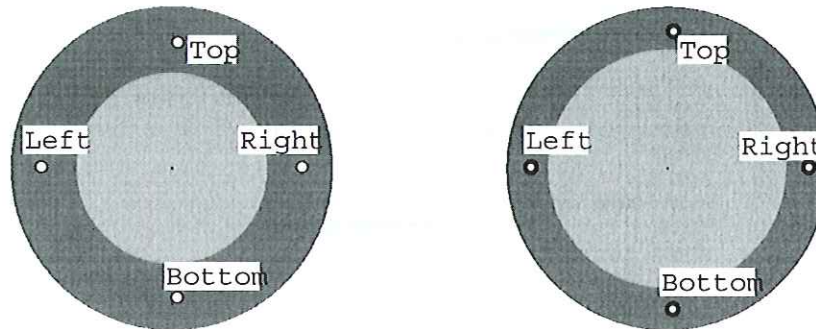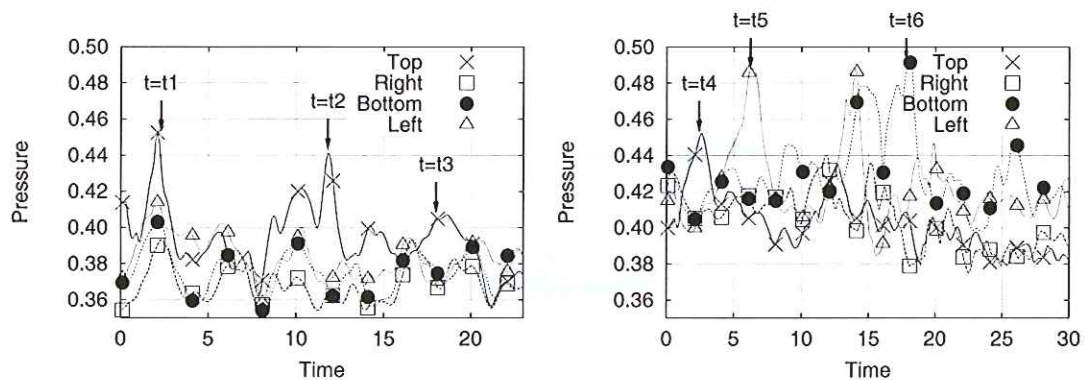
Fig. 19: Location of pressure ports.

Fig. 20: Time history of base pressure.

5.   FLOWFIELD AROUND THE CAPSULE AT FIXED PITCH ANGLE

The base pressure distributions for the D45 model (dynamically unstable) and D30 model (dynamically stable) fixed at $\alpha = 10°$ are discussed in detail in this section. Note that the capsules are not in the oscillation. The discussion in the previous section revealed that the mechanism of the flowfield is essentially the same for both the oscillating capsule and the fixed capsule. Therefore, it is possible to discuss the correlation between the flow structure and the dynamic stability of the capsule from the simulation of the flowfield around the capsule at a fixed pitch angle.

5.1   Unsteady base pressure distributions for capsule at fixed pitch angle

Time histories of the base pressure at 4 points on the base (locations shown in Fig. 19) for the two capsules are shown in Figs. 5.1 and 5.1.

The time-averaged base pressure for the D45 model at $\alpha = 10°$ is approximately 0.36 (Fig. 4.1), and instantaneous base pressure at the 3 points (Right, Bottom and Left) fluctuate within the range of 0.37 ± 0.01. The pressures at the point Top also fluctuate marginally around 0.38 for the most part, but occasionally rise to approximately 0.45. As the base pressure distribution
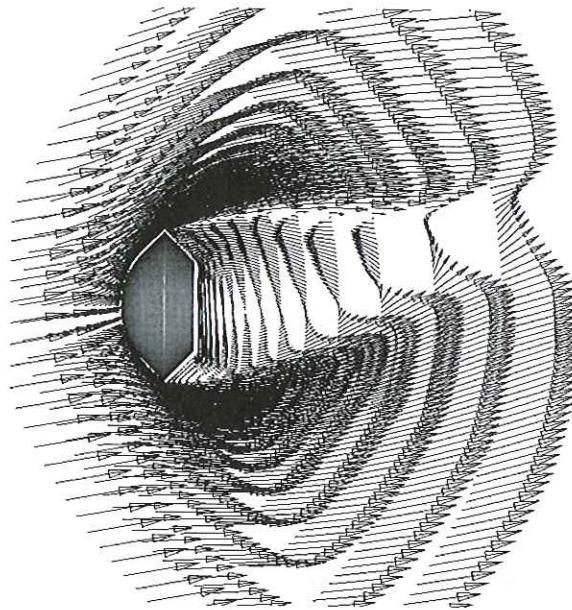
Fig. 21: Vector map in symmetry plane ($\alpha = 10°$, time-averaged).

for the D45 model is a superposition of a constant value and intermittent pressure peaks, the time-averaged pressure distribution depends on the behavior of the pressure peaks. The time-averaged pressure at the leeward (upper) side of the D45 model is higher because the pressure peaks appear only in the top region.

The base pressure for the D30 model is also expressed as the superposition of a constant value and intermittent pressure peaks as shown in Fig. 5.1. However, in this case the peaks appear randomly over the base, with the result that the time-averaged base pressure of the D30 model is almost uniform.

The difference in the characteristics of the time-averaged base pressure distribution reflects the difference in the unsteady behavior of the pressure peaks. Therefore, the flow mechanism that causes these pressure peaks is considered to be related to the dynamic instability of the capsule.

5.2 Correlation between base pressure and velocity field

Figure 21 shows the time-averaged velocity vectors in the plane of symmetry of the D45 model with pitch fixed at $\alpha = 10°$. A reverse flow region is observed behind the capsule with a maximum velocity of $u \simeq -0.5$. The non-dimensional density inside the recirculating region is $\rho \simeq 0.4$ and the resulting non-dimensional dynamic pressure is $\frac{1}{2}\rho u^2 \simeq 0.05$, which is consistent with the height of the pressure peaks in Figs. 5.1 and 5.1.

Figures 22 and 23 show the correlation between the reverse flow and the base pressure. The figures correspond to the instances when the pressure peaks, indicated by the arrows t1 ~ t6 in Fig. 20, appear on the base. The blue semi-transparent surface is the iso-surface of axial velocity $u = -0.4$, representing the core region of the reverse flow. The color of the capsule denotes the static pressure distribution. The contours of axial velocity are plotted on 3 planes, $x = 1.0$, 1.5 and 2.0. The contours are displayed only for the subsonic region, and therefore

the shapes of the contour planes represent the cross sections of the wake on each plane.

The high-pressure regions at the base (yellow and red area) always appear at the head of the reverse flow. For the D45 model (Fig. 22), the reverse flow passes the upper side of the wake and the high-pressure spot always appears at the point Top part of the base. On the other hand, the reverse flow of the D30 model (Fig. 23) passes the upper side when the high-pressure spot appears at the point Top ($t = t4$), the left side when the high-pressure spot appears at the point Left ($t = t5$), and the lower side when the high-pressure spot appears at the point Bottom ($t = t6$). These figures indicate that the high-pressure spots are caused by the impingement of the reverse flow against the base.

The primary difference between the reverse flows of the two capsules is their downstream position. The reverse flow of the D45 model passes the upper side of the wake at all three cross-sections, while the flowfield behind the D30 model is essentially axisymmetric even for positive pitch angles and the reverse flow passes almost through the center of the wake at sections $x = 1.5$ and 2.0.

5.3   Vortex structure behind the capsule

Time-averaged streamlines

Figure 24 shows the time-averaged streamlines behind the capsules fixed at a pitch angle $\alpha = 10°$. Two-dimensional time-averaged streamlines in the plane of symmetry are shown in Fig. 25.

A pair of large vortices is observed behind the D45 model (Fig. 5.3). The vortices are the counterclockwise vortices observed from the left side (Fig. 5.3), and push the reverse flow upward. The streamlines behind the D30 model (Fig. 5.3) are distorted almost randomly, and no clear flow structure is observed from the streamlines. In Fig. 5.3, the upper vortex (clockwise) and lower vortex (counterclockwise) are the same size, and the flowfield behind the D30 model is almost axisymmetric even though the capsule has non-zero pitch angle.

It becomes clear that the flow structure that makes the wake asymmetric and shifts the reverse flow upward is the pair of vortices behind the capsule.

Vortex core

As the three-dimensional structure of the vortices behind the capsule is difficult to recognize in the two-dimensional pictures of the streamlines (e.g. Figs. 24), the behavior of the vortices behind the capsule was discussed based on the two-dimensional streamlines in the plane of symmetry (Fig. 25) in the previous section. The vortex-core identifying technique developed by Sawada (Sawada, 1995) is applied here for discussion of the three-dimensional structure of the vortices. The method locates the core of the vortices automatically based on a critical-point analysis, and visualizes the vortices as the locus of the vortex core, providing a clearer view of the vortex structure than the streamlines. Figure 26(d) shows the locus of the vortex core behind the D45 model fixed at $\alpha = 10°$. The arrows in the figure denote the direction of propagation of the vortices. Figures 26(a)~(c) show the two-dimensional streamlines inside each cross section.

The vortex behind the capsule is composed of a distorted ring vortex and a pair of longitudinal vortices that emanates from the kink of the ring vortex. The ring vortex corresponds to the reverse flow, as shown in section (a), and the two contra-rotating vortices observed in Fig. 25 are in fact the cross sections of the single ring vortex. The behavior of the reverse flow is
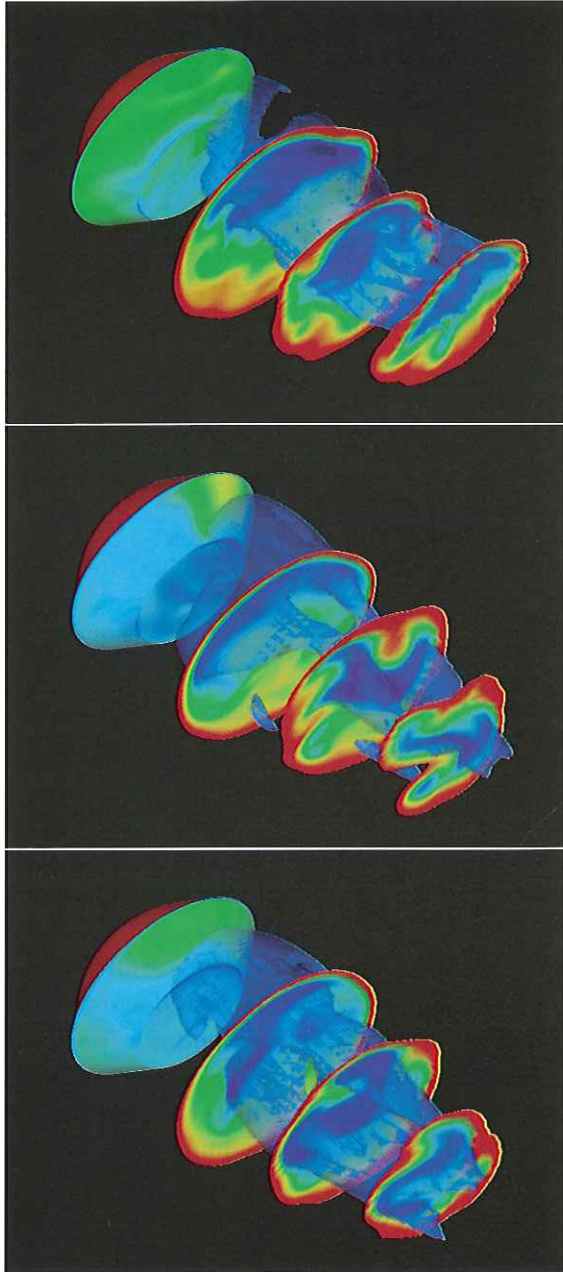
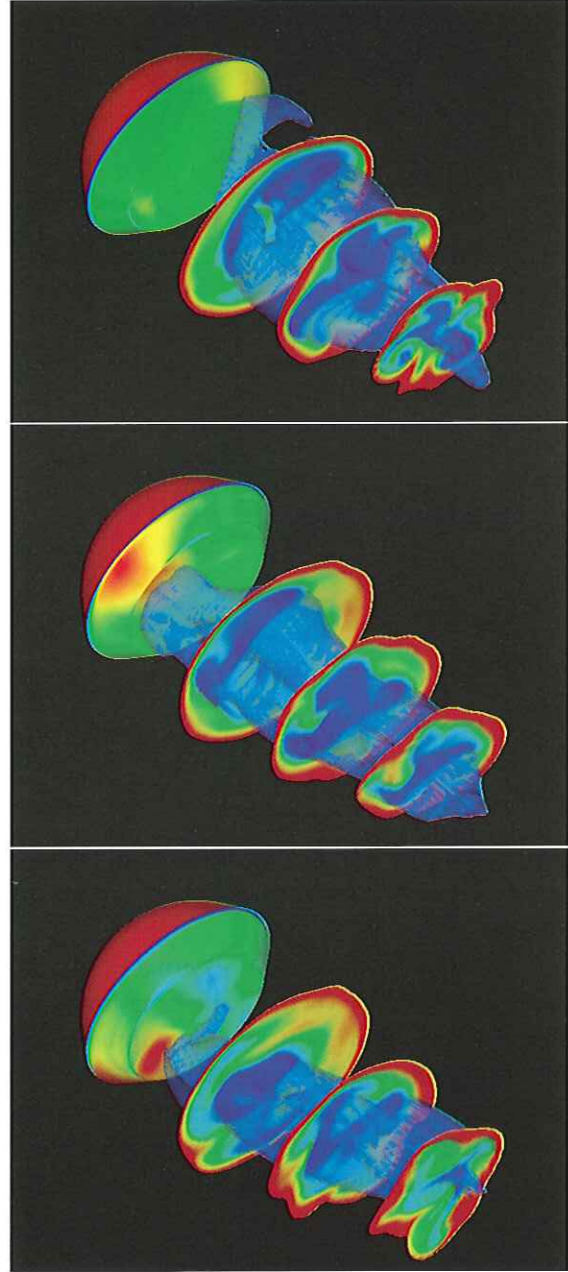Fig. 22: Reverse flow and base pressure (D45 model, $\alpha = 10°$).

Fig. 23: Reverse flow and base pressure (D30 model, $\alpha = 10°$).
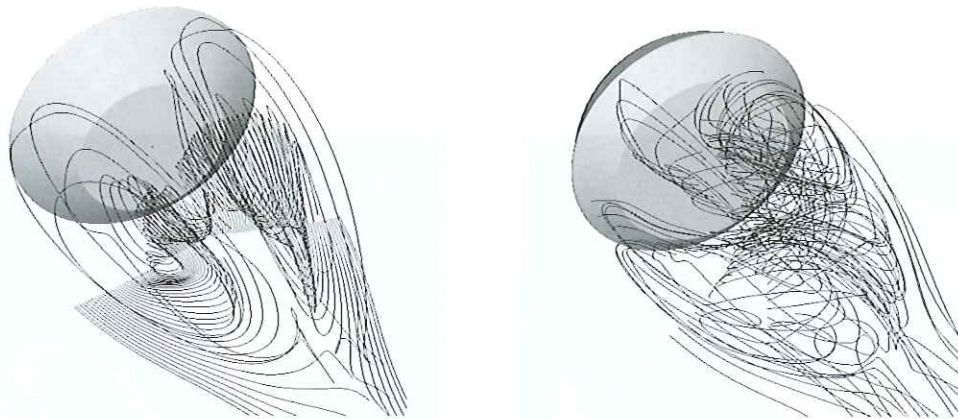
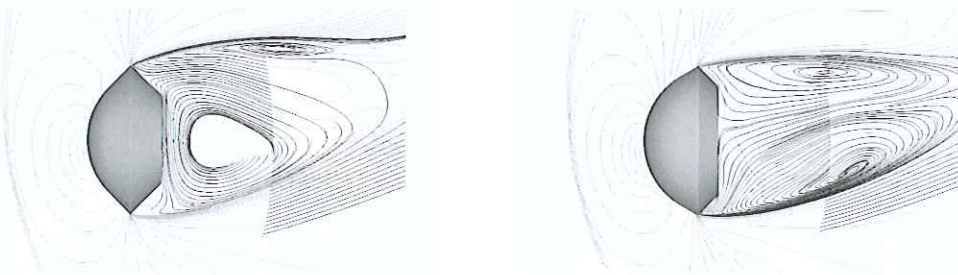Fig. 24: Streamlines behind capsule ($\alpha = 10°$, time-averaged).

Fig. 25: Streamlines in symmetry plane ($\alpha = 10°$, time-averaged).

correlated with the shape of the ring vortex: when the lower part of the ring vortex is located forward, the reverse flow is directed upward, passes the upper side of the wake and impinges on upper part of the base.

The vortices in section (c) are a pair of longitudinal vortices. The right vortex rotates clockwise, and the left vortex rotates counterclockwise, and both vortices propagate downstream. The vortices in section (b) also appear to be longitudinal vortices, yet are actually parts of the distorted ring vortex. Although the vortices in sections (b) and (c) are separate vortices, both rotate in the same direction and emanate from the neck point at which the shear layer converges. It appears that the vortices in sections (b) and (c) are both induced by the flow structure at the neck point.

Pair of longitudinal vortices

The discussions so far have focused mainly on the flow structure inside the recirculating region. Figure 27 shows a sideview of the streamlines inside the shear layer surrounding the recirculating region. The flow structure inside the shear layer is also shown schematically in Fig. 28.

The flow inside the shear layer is directed upward at the neck point. The upswept flows induce the pair of longitudinal vortices downstream, and also cause the ring vortex inside the recirculating region to deform. These figures show that the upswept flows at the neck point are closely related to the vortex structure discussed in the previous section.
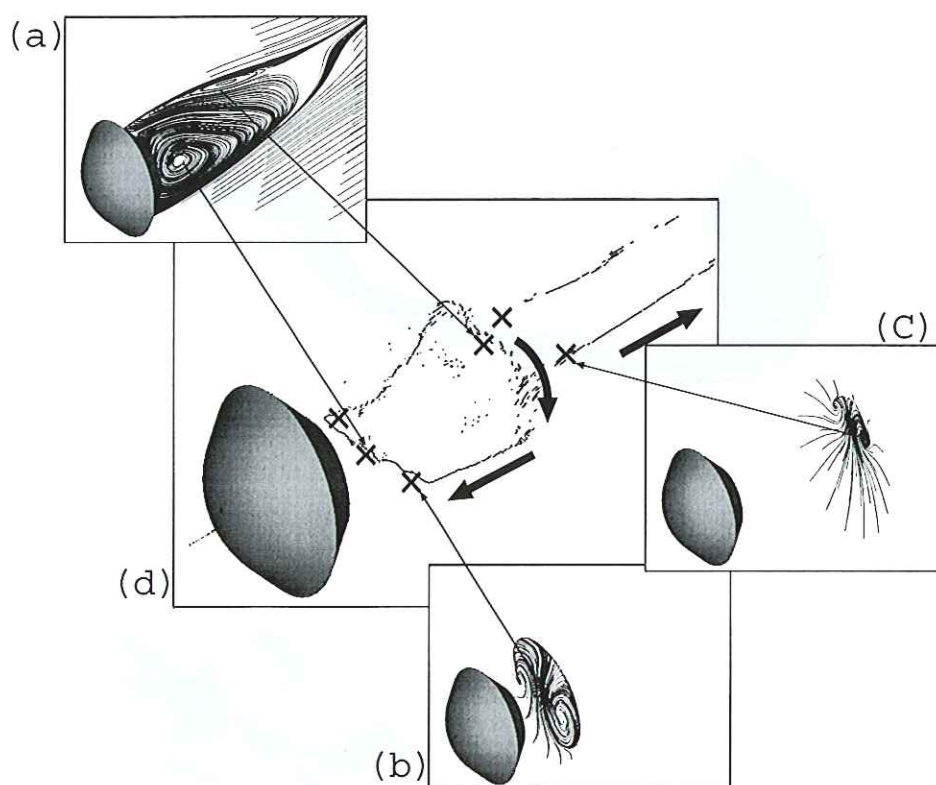
Fig. 26: Locus of vortex core ($\alpha = 10°$, time-averaged).

The upswept streams are formed by the convergence of upstream streamlines. In Fig. 27, the streamlines are directed slightly downward between the capsule and the neck point, and converge at the lower part of the neck point, there rolling up to form the upswept flows. The direction and convergence of the streamlines between the capsule and the neck point appears to be the key factor determining the flow structure behind the capsule.

6. Mechanism of dynamic instability

It has been found that the flowfield behind the oscillating capsule can be approximated by the constant-delay model, and that the flowfield is governed by the deformed ring vortex and the pair of longitudinal vortices.

Considering that the dynamic instability of the capsule is caused by the delay of the base pressure, the mechanism of the dynamic instability can be summarized as follows.

When the pitch angle of the capsule is changed, the base pressure does not change until the effect of the change in pitch angle reaches the base through the following four steps.

1. The pressure field at the front of the capsule changes immediately when the attitude of the capsule changes. The pressure field rotates the flow inside the shear layer behind the capsule downward, and the disturbance in the direction of the streamline propagates downstream.

2. The streamlines directed downward converge at the rear end of the recirculating region
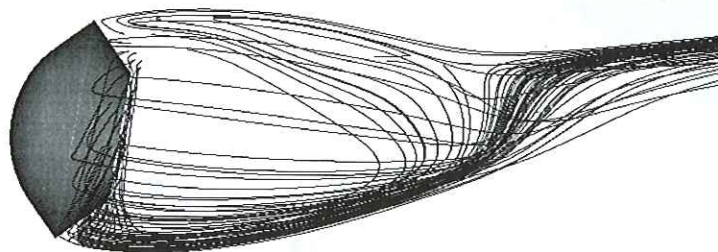
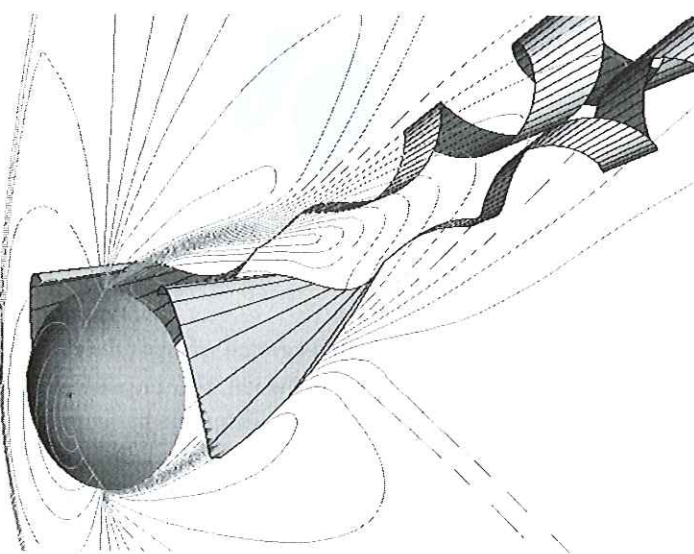Fig. 27: Streamlines inside shear layer ($\alpha = 10°$, time-averaged).

Fig. 28: Schematic view of longitudinal vortex pair.

(neck point). The streamlines then roll up and form upswept flows. The formation of the upswept flows near the neck point is delayed slightly with respect to the motion of the capsule since the speed of propagation inside the shear layer is finite.

3. The roll-up generates a pair of longitudinal vortices both upstream and downstream. The upstream longitudinal vortices distort the ring vortex behind the capsule and shifts the reverse flow upward.

4. The reverse flow impinges on top of the base, and the surface pressure at the upper part of the base becomes higher than the lower part. The change in base pressure distribution gives rise to pitch-down moment.

From these mechanisms we derive $\delta_b > 0$ and $\left.\frac{\partial M_{b\text{fixed}}}{\partial \alpha}\right|_\alpha < 0$. Equation (8) shows that the capsule is dynamically unstable when $\delta_b \left.\frac{\partial M_{b\text{fixed}}}{\partial \alpha}\right|_\alpha < 0$. Therefore, the capsule is dynamically unstable until a certain pitch angle is reached.

Under this mechanism, the delay of the base pressure reflects the propagation of the downward velocity component inside the shear layer from the edge of the capsule to the neck point. The speed of propagation and the distance between the capsule and the neck point are considered to be proportional to the freestream velocity U_∞ and the diameter of the capsule D, respectively. Therefore, the delay time δ is proportional to D/U for a given capsule shape and is independent of the frequency of the pitching oscillation. The phase angle ϕ is given by $\phi = 2\pi f\delta$, and the delay phase angle should be proportional to the frequency f. Additional simulations were carried out to verify this hypothesis (Teramoto and Fujii, 2002), and the results were consistent with the hypothesis.

7. Conclusion

The flowfields around blunt capsules, that represent the reentry capsule used in sample-return missions, were numerically studied in order to better understand the mechanism of dynamic instability of the capsule at transonic speeds.

The flowfield around the capsule in the forced pitching oscillation was numerically simulated. The results indicated that the oscillation of the base pressure is slightly delayed from that of the pitch angle, while the foreside surface pressure varies synchronously with the pitch angle. The base pressure, the recompression shock wave, and the wake near the neck point all oscillate with the same delay time, and the oscillation of the base pressure is considered to be coupled with the flowfield around the neck point.

The flowfield around the capsule at a fixed angle of attack was compared with that around the capsule under pitching oscillation. The change in the distribution of the surface pressure was essentially the same for the two flowfields except for a slight time delay at the base. The surface pressure of the oscillating capsule was modeled by a simple constant-delay model, and the dynamic stability of the capsule was discussed based on this model. It was shown that the dynamic stability of the capsule depends mainly on the behavior of the base pressure, and that the capsule is dynamically unstable when the change in the pitch-down moment induced by the base pressure distribution at positive pitch angle, is delayed with respect to the change in the pitch angle.

The characteristics of base pressure were discussed based on a simulation of the flowfield around the capsule at fixed pitch angles. There is strong reverse flow behind the capsule, and the impingement of the reverse flow on the base determines the base pressure distribution. The flowfield behind the capsule is characterized by a vortex composed of a ring vortex and a pair of longitudinal vortices. The longitudinal vortices induce upswept flows at the neck point when the capsule pitches up, the upswept flows push the reverse flow upward, and the change in the base pressure distribution produces a pitch-down moment. The base pressure does not change due to the change in pitch angle of the capsule until the change of the longitudinal vortices as a result of the attitude change propagates downstream and reaches the neck point. This time lag causes the phase delay of the base pressure.

The base pressure distribution and delay are closely related to the behavior of the pair of longitudinal vortices, and therefore the dynamic stability of the capsule is considered to be related to the formation of the pair of the longitudinal vortices downstream.

The mechanism of dynamic instability derived in this study reasonably explains the major features observed in the numerical simulations and is consistent with several important features reported in previous experiments.

ACKNOWLEDGMENT

REFERENCES

Baldwin, B. S. and Lomax, H. (1978). Thin layer approximation and algebraic model for turbulent flows. AIAA Paper 78-257.

Berner, C. and Winchenbach, G. L. (1998). A numerical and experimental investigation of generic space probes. AIAA Paper 98-0798.

Chapman, G. T. and Yates, L. A. (1998). Dynamics of planetary probes: Design and testing issues. AIAA Paper 98-0797.

Hiraki, K., Inatani, Y., Ishii, N., Nakajima, T., and Hinada, M. (1998). Dynamic stability of MUSES-C capsule. In *21st International Symposium on Space Technology and Science*. ISTS-98-d-33.

Obayashi, S., Matsushima, K., Fujii, K., and Kuwahara, K. (1986). Improvements in efficiency and reliability for Navier-Stokes computations using the LU-ADI factorization algorithm. AIAA Paper 86-0338.

Sammonds, R. I. and Kruse, R. L. (1975). Viking entry vehicle aerodynamics at M=2 in air and some preliminary test data for flight in CO_2 at M=11. NASA Technical Note NASA TN D-7974.

Sawada, K. (1995). A convenient visualization method for identifying vortex cores. *Trans. Japan Soc. Aero. Space Sci.*, 38(120):102–120.

Shima, E. and Jounouchi, T. (1997). Role of CFD in aeronautical engineering (No. 14) - AUSM type upwind schemes -. In *Proceedings of the 14th NAL Symposium on Aircraft Computational Aerodynamics*, pages 7–12, Tokyo, Japan. NAL.

Teramoto, S. and Fujii, K. (2001). Preprocessed visualization of large scale unsteady flow simulations. *Journal of Visualization*, 3(4):313–322.

Teramoto, S. and Fujii, K. (2002). Mechanism of dynamic instability of a reentry capsule at transonic speeds. *AIAA Journal*, 40(12). to be published.

Teramoto, S., Hiraki, K., and Fujii, K. (2001). Numerical analysis of dynamic stability of a reentry capsule at transonic speeds. *AIAA Journal*, 39(4):635–642.

Wright, B. R. and Kilgore, R. A. (1966). Aerodynamic damping and oscillatory stability in pitch and yaw of Gemini configurations at Mach numbers from 0.50 to 4.63. NASA Technical Note NASA TN D-3334.

Yoshinaga, T., Tate, A., Watanabe, M., and Shimoda, T. (1996). Orbital re-entry experiment vehicle ground and flight dynamic test results comparison. *Journal of Spacecraft and Rockets*, 33(5):635–642.